RESEARCH PAPER

Magnetophoretic mixing for in situ immunochemical binding on magnetic beads in a microfluidic channel

Ranjan Ganguly · Thomas Hahn · Steffen Hardt

Abstract Functionalized magnetic beads offer promising solutions to a host of micro-total analysis systems ranging from immunomagnetic biosensors to cell separators. Immunochemical binding of functional biochemical agents or target biomolecules serves as a key step in such applications. Here we show how magnetophoretic motion of magnetic microspheres in a microchannel is harnessed to promote in situ immunochemical binding of short DNA strands (probe oligonucleotide) on the bead surface via streptavidin–biotin bonds. Using a transverse magnetic field gradient, the particles are transported across a co-flowing analyte stream containing biotinylated probe oligonucleotides that are labeled with a Cy3-fluorophore. Quantification of the resulting biotin–streptavidin promoted binding has been achieved through fluorescence imaging of the magnetophoretically separated magnetic particles in a third stream of phosphate buffered saline. Both the experimental and numerical data indicate that for a given flow rate, the analyte binding per bead depends on the flow fraction of the co-flowing analyte stream through the microchannel, but not on the fluid viscosity. Parametric studies of the effects of fluid viscosity, analyte flow fraction, and total flow rate on the extent of binding and the overall analyte separation rate are also conducted numerically to identify favorable operating regimes of a flow-through immunomagnetic separator for biosensing, cell separation, or high-throughput applications.

Keywords Magnetic microspheres · Microfluidics · Micromixing · Immunochemical Binding · Lagrangian Particle Tracking

R. Ganguly
Department of Power Engineering, Jadavpur University, Kolkata 700098, India

R. Ganguly
Institute for Nano- and Micro Process Technology, Universität Hannover, 30167 Hannover, Germany

T. Hahn · S. Hardt (✉)
Center of Smart Interfaces, TU Darmstadt, 64287 Darmstadt, Germany
e-mail: hardt@csi.tu-darmstadt.de

1 Introduction

In micro-total analysis systems (μ-TAS) (Manz et al. 1990) (bio)analytical protocols are implemented on microfluidic chips. Compared to standard laboratory-scale systems, these devices have a highly reduced size and weight and are capable of performing all sample handling steps (e.g., mixing, incubation, separation) along with analytical measurements on a single platform (Greenwood and Greenway 2002). μ-TAS can combine multiple steps of a detection protocol on a single chip, reduce the overall analysis time and minimize the consumption of expensive reagents. Achieving adequate mixing is one major challenge faced by μ-TAS, since they operate with very low Reynolds number flows, and the molecular diffusivity of the large organic molecules they handle is very low. Thus, the biochemical reaction rates are generally limited by the extremely large diffusion time scales. Enhancement of chemical reactions in a μ-TAS can be accomplished through artificially increasing the mixing rate and/or providing large reactive surfaces. Several passive and active mixing techniques have been studied by researchers to enhance mixing in microfluidic devices (Nguyen and Wu 2005; Hardt et al. 2006; Jiang et al. 2004; Wu and Li 2008; Roy et al. 2009). While most of the standard passive mixing strategies warrant complicated

microfluidic architectures, active mixing strategies generally involve complex operations.

Magnetic bead-based immunoassays offer a promising solution for MEMS-based biosensing applications. Magnetic microspheres typically used in that context are 1–2 μm diameter polystyrene beads impregnated with superparamagnetic nanoparticles ($\sim$10 nm in diameter). The beads can be steered easily and precisely by a suitably imposed magnetic field gradient in the microfluidic environment. By functionalizing the bead surfaces with suitable bioconjugates, the microspheres can be attached to cells, DNA or antibodies with high selectivity, making it possible to manipulate cells or biomolecules with external magnetic fields (Radbruch et al. 1994; Tibbe et al. 2002; Xia et al. 2006; Pamme and Manz 2004). The motion of an ensemble of magnetic microspheres in a microfluidic channel can be controlled in a manner that the particle–fluid hydrodynamic interaction augments mixing. Since these beads can offer a large specific surface for chemical binding, they can be advantageously used as a "mobile substrate" for microscale bio-assays. It is intuitive that a great deal of device-level complexity could be avoided if the same magnetic beads used as mobile substrates in the biosensor could also be used for enhancing mixing. An in situ immunochemical binding of analytes on the beads eliminates the need for a separate bead-incubation arrangement. The concept is particularly useful in multiplexed diagnostic system, where the magnetic beads from a single reservoir can be flown through several parallel channels where they immunochemically bind in situ with several different (target or probe) analytes.

The literature on magnetic bead-based mixers has proposed a wide variety of solutions with their own pros and cons. Efficient mixing strategies using rotating chains of magnetic microspheres for flow-through systems (Biswal and Gast 2004) and microdroplets (Roy et al. 2009) have been demonstrated, but they required elaborate on-chip or off-the chip arrangements for generating rotating magnetic fields. Suzuki et al. (2004) proposed a magnetic bead-based chaotic mixer that required complicated channel architecture. A numerical study by Wang et al. (2008) showed that the magnetic particles could be steered in a microchannel using a carefully modulated alternating magnetic field so that the coupled particle–fluid momentum exchange enhances mixing in a microchannel. However, Modak et al. (2009) have shown that the extent of momentum coupling (and hence the mixing index) is poor for low number density of particles, implying that these strategies may not be feasible for low bead concentration applications. Hayes et al. (2001) proposed a small-volume heterogeneous immunoassay where the analyte sample was perfused through a magnetically immobilized plug of magnetic bead to promote on-bead binding. Rida and Gijs (2004), Lund-Olesen et al. (2008), and Moser et al. (2009) have further improved this

concept by using an ac-magnetic field-modulated dynamic plug of beads to enhance mixing and analyte binding. A similar approach by Lacharme et al. (2008, 2009) uses self-assembled chains of magnetic beads placed across the flow in a periodically structured microchannel to improve bead–analyte contact. However, besides having complicated geometry, and a widely varying extent of analyte binding on the particles (the far downstream chains have nearly one-tenth the analyte binding on the first chain in the flow), the flow velocity in these devices are severely restricted by the stability of the magnetic particle chains. A much simpler configuration, using a static magnetic field, is proposed in a more recent numerical analysis (Baier et al. 2009) where cross-stream mixing between two co-flowing streams of magnetic particles and analyte, and the immunomagnetic separation of cells in a tapered microchannel have been characterized. However, an experimental characterization of an in situ immunochemical binding in a similar flow-through microchannel is, to the authors' best knowledge, not available in the literature. The task of transporting particles crossing the streamlines in a microfluidic configuration is also achieved by other techniques like dielectrophoresis (DEP) (Kang et al. 2008, 2009) or asymmetric post arrays (Morton et al. 2008), but they involve complicated micro-fabrication issues (e.g., embedded electrodes or dielectric obstacles for DEP or the asymmetric post array). The operational challenges (e.g., electrical field response of the biological entities, electrolysis, gas generation, clogging, etc.) are also either absent or minimal with the present device. Besides, the magnetophoretic device proposed here can also act as an in situ collector of the labeled particles in the form of an aggregate (which can later be re-suspended in the same microchannel by magnetic or hydrodynamic action and used for a subsequent analysis step), which is not feasible with asymmetric post arrays.

Herein we show a scheme of achieving cross-stream mixing and in situ immunochemical binding of biotinylated short DNA chains (oligonucleotides) on streptavidin-functionalized magnetic beads in a flow-through microfluidic channel using a transverse magnetophoretic transport of the beads. The streptavidin–biotin combination is used, since it is one of the most common types of immunoassay used in microfluidic applications. The 22 bases probe oligonucleotide chosen for the experiments encodes the ΔF508-mutation in the transmembrane conductance regulator (CFTR), a genetic disorder accountable for 70% of the cystic fibrosis cases (Cystic Fibrosis Mutation Database, URL: http://www.genet.sickkids.on.ca/cftr) which is herein an example for any sequence that can be investigated. The transport of the magnetic beads through the co-flowing stream of analyte is described to explain the mechanism of immunochemical binding on the bead surface. The extent of immunochemical binding on the bead surfaces is quantified

through laser-induced fluorescence. Experimental findings are analyzed in the light of a first-order scaling analysis and also through Lagrangian tracking (Sinha et al. 2007) of the magnetic particles in the pressure driven flow environment. The effect of varying the operating parameters on the in situ biochemical reaction is also studied in the context of the different requirements for microfluidic devices employing in situ immunochemical binding. The proposed mixing strategy can be implemented in either (i) an in-line separation unit of a magnetoresistance-based biosensor in which the functionalized beads attach to a "target analyte" present in the background fluid in an extremely low concentration, and are then targeted on functionalized magnetoresistive sensors to form a sandwich immunoassay (Graham et al. 2004), (ii) an in-line bead incubator, where a specified amount of beads is to be functionalized with a "probe oligonucleotide," which can be subsequently used to detect a target analyte (Rong et al. 2006), or (iii) a high-throughput immunomagnetic separation unit (Yung et al. 2009). The device requirements for the three applications are different. For example, the average analyte binding per single bead is of primary importance for the first application, since the sensitivity of the device depends largely on how many target molecules a bead can attach to, before entering the detection unit. Magnetoresistance-based sensors can detect even the presence of a single magnetic bead (Graham et al. 2004), but such a detection is possible only if the bead has bonded to a large enough number of target analyte molecules so that it would attach to the functionalized magnetoresistive sensor probe. The second application requires not only a high binding per bead, but also a high separation efficiency of the functionalized beads from the background fluid. Thus, for comparing the device performances for such applications, the product of per bead binding and the particle capture efficiency is of relevance. Lastly, for high-throughput devices, the rate of separation of the total analyte is important, so that the device performance will depend on per-bead analyte binding, the particle capture (or separation) efficiency and the bead/analyte supply rate. We have investigated the parametric variation of our immunomagnetic assay considering these three attributes.

2 Materials and methods

### 2.1 Principle of magnetophoretic mixing and immunochemical binding

Figure 1a shows a schematic diagram, explaining the principle of magnetophoretic mixing inside the microchannel. The functionalized beads and the probe oligonucleotide (which has a binding affinity toward the functionalizing molecules on the beads) are passed through

the channel in co-flowing streams B and C, respectively. In the absence of any magnetic field, there is very little cross-stream mixing. Because of the extremely low diffusivities of the beads and oligonucleotides, the extent of binding between both is very small, and it remains confined within an extremely narrow mixing region at the interface of the streams B and C. When a cross-stream magnetic field gradient is imposed (e.g., by a permanent magnet or electromagnet), the magnetic beads experience magnetic and hydrodynamic drag forces, $\mathbf{F}_m$ and $\mathbf{F}_d$, and a gravitational force $\mathbf{F}_g$ (Ganguly and Puri 2007). Applying Newton's second law of motion for a magnetic particle,

$$\left(\tfrac{4}{3}\pi a^3 \rho_p\right)d\mathbf{V}_p/dt = \left[\mathbf{F}_m + \mathbf{F}_d + \mathbf{F}_g\right] \qquad (1)$$

where the force terms are expressed as

$$\mathbf{F}_m = \mu_0\left(\tfrac{4}{3}\pi a^3\right)\left[\chi \middle/ \left(1 + \tfrac{1}{3}\chi\right)\right]\tfrac{1}{2}\nabla(\mathbf{H}_0 \cdot \mathbf{H}_0), \qquad (2)$$
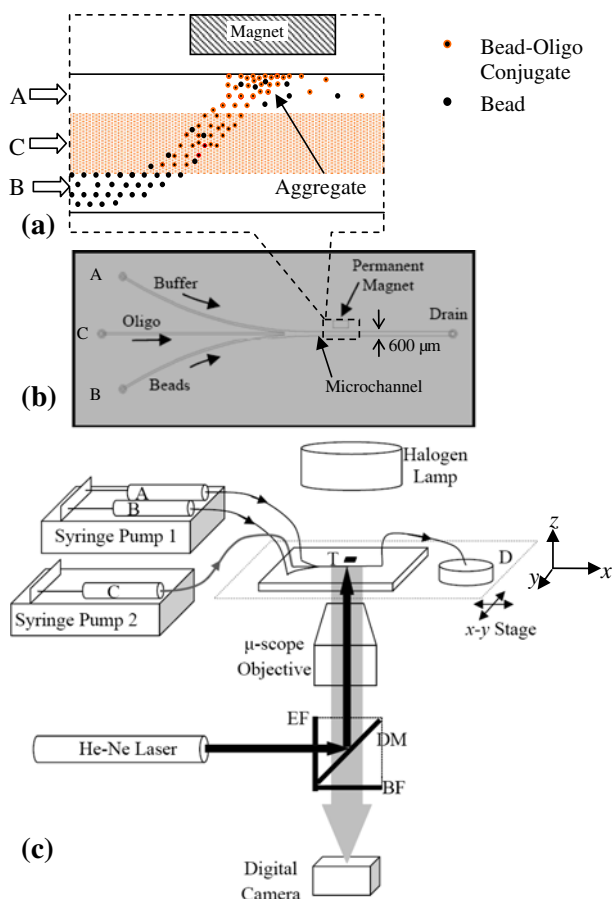
Fig. 1 a Principle of the cross-stream mixing in microchannel. **b** The PMMA chip with 600 μm (width) × 120 μm (depth) × 3,000 μm (length) test section. **c** The flow system and the epifluorescence microscopy arrangement. *Legend*: *A* buffer solution, *B* streptavidin coated beads, *C* Cy3-labeled oligonucleotide, *D* drain, *T* test section, *EF* emission filter, *DM* dichroic mirror, *BF* barrier filter

$$\mathbf{F}_d = 6\pi a\eta(\mathbf{V}_1 - \mathbf{V}_p), \tag{3}$$

and

$$\mathbf{F}_g = \left(\frac{4}{3}\pi a^3\right)(\rho_p - \rho_1)g. \tag{4}$$

Here, a denotes the particle radius, χ the intrinsic magnetic susceptibility of the bead, g the acceleration due to gravity, $\mathbf{V}_p$ and $\mathbf{V}_1$ denote the absolute velocities, and ρ_p and ρ_1 the densities of the particles and carrier liquid, respectively. The fluid viscosity is denoted by η and $\mathbf{H}_0 = (\mathbf{B}_0/\mu_0)$, while $\mathbf{B}_0$ denotes the local magnetic field due to the external magnet and μ_0 the vacuum permeability. The expression of the magnetic force in Eq. 2 arises from the integration of the Kelvin body force over the particle volume, i.e., $\mathbf{F}_m = \mu_0\int(\mathbf{M}\cdot\nabla)\mathbf{H}d\vartheta = \mu_0\left(\frac{4}{3}\pi a^3\right)(\mathbf{M}\cdot\nabla)\mathbf{H}$, and takes into account a demagnetization factor arising from the distortion of the externally imposed magnetic field by the induced magnetic field of the particle (Smistrup et al. 2005). Because of the extremely small inertia of the 1 μm radius magnetic particles, the left hand side of Eq. 1, can be neglected. Thus, the equation of motion of the magnetic beads reduces to

$$\mathbf{V}_p = \mathbf{V}_1(y,z) + \frac{(\mathbf{F}_m + \mathbf{F}_g)}{6\pi a\eta}. \tag{5}$$

The velocity of the host fluid at any cross-sectional plane (y, z) (see the coordinate frame in Fig. 1c for reference) in a fully developed pressure-driven flow through the microchannel of width h (the y dimension) and depth b (the z dimension) obeys the infinite Fourier series solution of the Navier–Stokes equation (Ichikawa et al. 2004), so that

$$\mathbf{V}_1(y,z) = \left(\frac{Gb^2}{8\eta}\right)\frac{32}{\pi^3}\sum_{n=0}^{\infty}\left(\frac{(-1)^n}{(2n+1)^3}\right)$$
$$\times \left\{1 - \frac{\cosh\left[\frac{(2n+1)\pi y}{b}\right]}{\cosh\left[\frac{(2n+1)\pi h}{2b}\right]}\right\}\cos\left[\frac{(2n+1)\pi z}{b}\right]\hat{i}. \tag{6a}$$

Here G denotes the axial pressure gradient $(-dp/dx)$, and is related to the average flow velocity as

$$G = u_{av}\left(\frac{\pi^4\eta}{8h^2}\right)\bigg/\sum_{n=0}^{\infty}\frac{1}{(2n+1)^4}$$
$$\times\left\{1 - \frac{2b}{(2n+1)\pi h}\tanh\left[\frac{(2n+1)\pi h}{2b}\right]\right\} \tag{6b}$$

The gravity-induced settling in a sufficiently short microchannel can be insignificant when the beads are small and their density is close that of the background fluid. This is also verified in our experiment, where no noticeable

gravitational settling of particles in the test section of the microchannel has been observed. Therefore, the only significant force term of Eq. 5 is $\mathbf{F}_m$. Because of the magnetic force, the magnetic beads acquire a transverse magnetophoretic velocity and pass over the stream C. This enhances the bead–oligonucleotide interaction and surface binding. When the magnetic field gradient is strong enough, the magnetic beads are immobilized on the wall of the microchannel, where the magnetic field gradient is the largest (Fig. 1a). When the number density of captured beads close to the wall increases, the magnetic beads also develop a strong particle–particle interaction, leading to the formation of a stable aggregate. Since the cross-stream mixing between the beads and the oligonucleotides is conducive for their binding, the aggregate is rich in bound molecules of C. A stream of buffer A separates the aggregate from the stream C, and can be used for post-capture removal of the bead–analyte conjugates to the downstream once the magnetic field is withdrawn.

The extent of cross-stream mixing is quantified through a study of the immunochemical binding between streptavidin coated beads (stream B) and a fluorophore-labeled biotinylated probe oligonucleotide (stream C). Due to the biotin–streptavidin binding, the beads pick up fluorescence as they pass over the stream C and deposit on the channel wall near the magnet. The better the binding, the larger is the fluorescence exhibited by the magnetically immobilized bead aggregate.

2.2 Materials

Polymer-based streptavidin-coated magnetic beads (Micromer-M, Micromod Partikeltechnologie GmbH, URL: http://micromod.de), having a mean diameter of 2 μm, density of 1,100 kg/m³, magnetization of 3.3 kA/m at 0.1 T (corresponding to an intrinsic magnetic susceptibility of 0.04), and saturation magnetization $M_{sat} = 3.96$ kA/m, are used for the experiment. Each bead has $\sim 10^5$ streptavidin molecules functionalized on its surface, providing an equivalent number of biotin binding sites. The beads are stabilized in phosphate buffered saline (PBS, pH = 7.4) at a loading of 25 mg/ml for storage. Before use, they are homogeneously suspended in PBS buffer at loadings of 0.2 or 0.625 mg/ml in an ultrasonic bath (VWR USC 300TH). The oligonucleotide sample has 22 base pairs (the sequence is 5′-AAT ATC ATT GGT GTT TCC TAT G-3′, with its 5-prime end biotinylated and the 3-prime end tagged with Cy3 fluorophores) and is obtained in 3× HPLC purity at 0.1 nmol/μl concentration (PURIMEX, URL: http://www.purimex.com/). The sample is further diluted in PBS (pH = 7.4) to 0.25 nmol/ml before introducing it into the microchannel. The Cy3 fluorophores, having an absorption maximum at 552 nm and an emission

maximum at 570 nm, are used for tagging the sample for laser-induced fluorescence imaging and quantification of immunochemical binding on the beads.

2.3 Chip

Microfluidic chips are fabricated on 3-mm thick PMMA plates by micromilling (LPKF ProtoMat® S100) the channels. Slots for inserting the permanent magnet are also milled into the PMMA substrate. Fluidic ports are drilled from the back side of the channel. The channels are covered with 500 μm thick PMMA sheets through solvent bonding. A NdFeB permanent magnet (IBS Magnet, remanence B_r = 1.17–1.25 T, relative remanent permeability 1.07) of 1 mm × 2 mm × 2 mm dimension is inserted into the slots on the chip, with one of its 2 mm × 2 mm pole faces placed 500 μm away from one wall of the microchannel. Figure 1b shows the schematic diagram of a typical chip used in this study. Samples are drawn through three inlet streams A, B, and C merge into a 600 μm × 120 μm × 3,000 μm straight channel (the test section), whose other end is connected to the drain D.

2.4 Experiment

Figure 1c shows the schematic diagram of the experimental setup. The chip is mounted horizontally on the micrometer stage of an inverted microscope (Nikon Eclipse TE 2000-E) for visualization. Images were acquired using a high-sensitivity monochrome digital camera (Nikon Digital Sight DS-Qi1Mc). Bright-field images are obtained under the microscope-mounted halogen lamps. For epifluorescence images, a He–Ne Laser (Melles Griot, 543.5 ± 5 nm, 1.5 mW) source is used in conjunction with a Nikon TRITC TIRF filter set. The laser passes through an excitation filter (EF: band pass 543 ± 5 nm) and reflects from a dichoric mirror (DM: near unity reflectivity below 550 nm and near-unity transmissivity above 570 nm) to shine on the test section T (Fig. 1c) through the microscope objective. The Cy3 fluorophores are excited under the 543 nm laser when they produce laser-induced fluorescence at a slightly larger wavelength (the Stokes shift for the Cy3 fluorophore is 18 nm, cf. Mullins 1999). The duration of laser illumination is limited through a separate shutter box (Nikon LUSU) so as to minimize photo-bleaching of the fluorophores. The fluorescent signal from the sample is transmitted down through the microscope objective, dichroic mirror, and the barrier filter (BF: band pass 585 ± 20 nm). Images are processed through an image analysis software (NIS-Elements, Nikon).

A pressure-driven flow is established through the chip using a pair of double-syringe infusion pumps (KD Scientific-201-CE). The flow rates of streams A and B are always maintained equal by supplying through the syringe pump 1 (Fig. 1b), while the flow in stream C is controlled through the second syringe pump. The viscosity of the background liquid (PBS buffer) in all the three streams is varied by premixing a measured amount of polyethylene glycol (MW 1000, Carl Roth GmbH).

2.5 Simulation

The magnetic field imposed by the permanent magnet is calculated by using Maxwell® v 12.1, which is a FEM-based computational software to solve the Maxwell equations of magnetostatics, e.g.,

$$\nabla \times \mathbf{H}_0 = 0, \quad \text{and} \quad \nabla \cdot \mathbf{B}_0 = 0. \tag{7}$$

The 3-d magnetostatic solver is used to compute the field in a 12 mm × 4 mm × 4 mm region containing the permanent magnet and the microchannel (the permeability of PMMA is assumed to be the same as that of the vacuum). For the specified dimensions and properties of the permanent magnet, the solution proceeds through 15 adaptive passes based on the principle of total energy error (TEE) minimization, refining the grid from 96 (TEE = 33.95%) to a total of 364,771 (TEE = 0.44%) tetrahedral elements. Subsequently, the converged magnetic field and gradient data in the computational zone of the microchannel are exported to a 3-d Cartesian grid of 5 μm resolution for the computation of the magnetic force components on the particles. Lagrangian tracking of the particles has been carried out using a numerical time integration of Eq. 5 following the Euler explicit method. The forward differencing time intervals dt in the simulation has been specified so as to limit the particle travel to a distance smaller than 1/1,000th of the channel width, i.e., $|\mathbf{V}_p| \cdot dt < h/1{,}000$. For the purpose of the simulation, 50 representative monodispersed particles are assumed to enter the domain from random (y, z) coordinates at the inlet plane of the stream B of the channel with zero slip velocity between fluid and particles (the initial condition for Lagrangian tracking). The intrinsic magnetic susceptibility is assumed at each time step for each particle as $\chi = 0.04$ for the local value of $|\mathbf{B}| \leq 0.124$ T (i.e., until the maximum particle magnetization $M_{sat} = 3.96$ kA/m is reached). Beyond this value, the particle magnetization is kept constant by treating $\chi = M_{sat}/|\mathbf{H}|$. The width of the stream B is computed from the fractional flow rates of the bead stream (f_{bead} = flow rate of stream B/total flow rate) and the Cy3 stream (f_{Cy3} = flow rate of stream C/total flow rate), based on the fully developed velocity profile of Eq. 6a.

3 Results and discussion

3.1 Magnetophoretic motion of beads in the channel

Particle trajectories in a magnetophoretic microsystem depend on the ratio of the magnetic to the viscous force (Nandy et al. 2008). Here we have considered a fixed magnetic configuration for which the computed field distribution within the microchannel (on the channel mid-plane perpendicular to the z axis) is described in Fig. 2. The permanent magnet imposes strong field gradients ($\sim$100–10 T/m) across the channel cross section on the x–y plane. Since the magnet is placed symmetrically with respect to the channel mid plane (perpendicular to the z axis), the field gradient perpendicular to the x–y plane is typically one order of magnitude smaller ($\sim$10–1 T/m).

For a given magnetic field distribution and fluid viscosity, the nature of the particle trajectories depend on the flow velocity in the channel. The left hand side panels of Fig. 3a–d show the experimentally observed particle trajectories (through long-exposure dark-field images recorded under the illumination of a halogen lamp shining from the sides) inside the channel for the average flow velocities of 290, 579, 868, and 1,157 μm/s, respectively (with equal flow rates in the streams A, B, and C). The right hand side panels of Fig. 3a–d show the corresponding trajectories obtained through numerical simulation for the same flow conditions, with $a = 2$ μm, and $\eta = 0.00089$ Pa s. For all of the flow regimes shown in Fig. 3a–d, the particles are found to be deflected toward the magnet, crossing the middle stream, and finally settling on the upper side-wall where the magnetic field is strongest (the position of the magnet is shown schematically). However, the curvatures of the trajectories differ as the flow velocity changes. Particle trajectories are also found to intersect each other (in both the experimental and computed pathlines), since particles enter the domain at different z-locations with different velocities. It is apparent from Fig. 3 that with increased flow velocity, the number of particles escaping

downstream increases. The average residence time of the particles in the middle stream (C) also changes with the flow velocities, which is discussed quantitatively in Sect. 3.5.

The particles captured on the wall are found to form an aggregate near the region of high magnetic field gradient. Figure 4 shows such an aggregate of beads that are immobilized on the wall. The size of the bead aggregate is found to depend on the particle loading in stream B, the fluid velocity and the duration of flow, since all three are related to the total number of particles in an aggregate. For the experimental diagnostics, we focus our analysis on this aggregate, since the fluorescence intensity of the aggregate is related to the extent of biochemical binding that has taken place on the surface of its constituent beads.

3.2 Aggregate growth rate

When a steady flow of the beads, the Cy3-labeled oligonucleotide and the buffer is maintained through the channel, the bead-aggregate on the wall grows in size with time. The aggregate shows fluorescence, since the beads bind with the Cy3-labeled target oligonucleotides through the streptavidin–biotin binding, while passing over the stream C. Figure 5a shows the fluorescence images ($4\times$ objective) of the aggregate for inlet bead concentrations of 0.625 and 0.2 mg/ml. Equal flow rates are maintained in the three streams, corresponding to an average flow velocity of $u_{av} = 579$ μm/s. The inset of the top frame of Fig. 5a shows enlarged views ($50\times$ objective) of the aggregate, where individual fluorescent beads are also visible. It is also evident from Fig. 5a that the cross-stream magnetophoretic motion of the beads leads to a better transverse (upward) dispersion of the oligonucleotides from the central (C) stream into the stream A. This can be attributed to the transverse advective component of the background fluid arising from the particle–fluid momentum exchange in the regions of upward trajectories of the beads (Modak et al. 2009) and leads to an additional advective supply of the fluorophore-labeled oligonucleotides toward the aggregate (which is otherwise isolated from the stream C by the buffer stream A). Therefore, in spite of a steady flow, one would expect that the average fluorescence intensity (intensity per pixel) of the aggregate to increase with time. This is corroborated from the average fluorescence intensity data shown in Fig. 5b. The average fluorescence intensity (qualitatively denoting the fluorescence per bead) is computed by averaging the intensity per pixel data from three representative regions of interest (ROI) of areas of 530, 288, and 462 μm^2 on the aggregate from a sequence of time-lapse images for the duration of 20 min. For both the bead concentrations the intensity per pixel is found to increase linearly with time. In Fig. 5b, the data of the first 200 s is discarded as until then the aggregate size
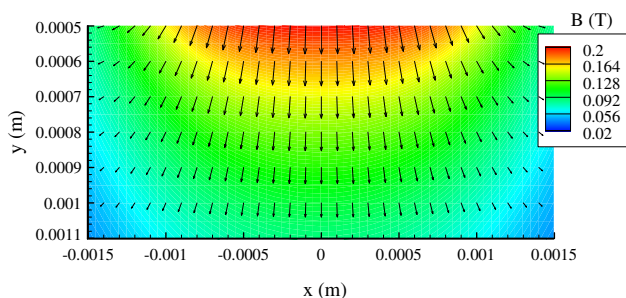
Fig. 2 The magnetic field distribution within the microchannel due to the permanent magnet (computed using Maxwell® v12.1, the magnet is placed between $x = -1$ mm and $x = 1$ mm, with one pole face at $y = 0$)

Fig. 3 **a**–**d** Long-exposure dark-field imaged (*left*) and numerically computed (*right*) particle trajectories under different average flow velocities: **a** 290 μm/s, **b** 579 μm/s, **c** 868 μm/s, and **d** 1157 μm/s. The magnetic particles are introduced in stream B. The flow rates of streams A, B, and C are identical
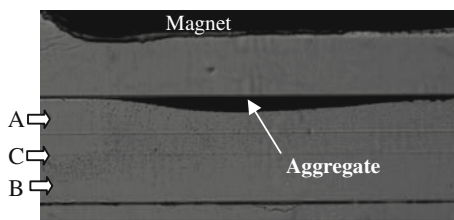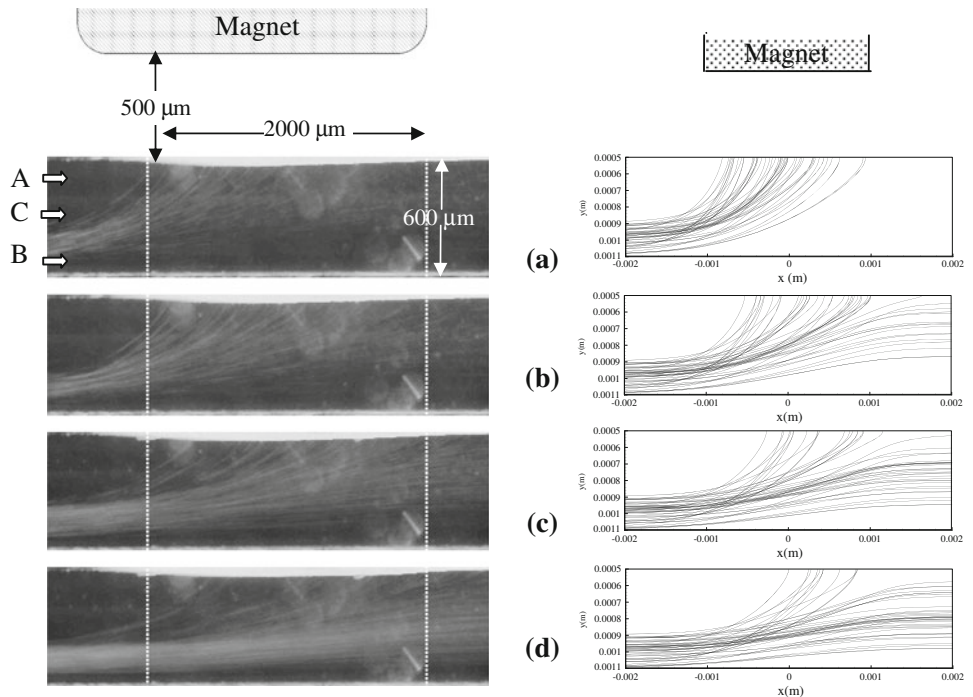
Fig. 4 Bright-field image of the magnetic bead aggregate (after 20 min of flow at 579 μm/s, with an inlet bead concentration of 0.625 mg/ml)

was not large enough to completely fill the ROIs chosen to compute the intensity per pixel data. It can be observed from Fig. 5b that the growth rate of average fluorescence intensity of the aggregate is approximately 1.75 times higher when the bead loading is increased from 0.2 to 0.625 mg/ml. This is due to the fact that a larger particle density implies a stronger particle fluid interaction during the magnetophoretic motion and hence a larger advective cross-stream mixing of the fluorophores.

3.3 Relating the fluorescence intensity to binding

In order to quantify the extent of streptavidin–biotin binding on the bead surface, it is essential to first know the maximum fluorescence intensity that a bead aggregate, saturated with the fluorophores, can produce. Although there are nearly 10^5 streptavidin site on each bead, the actual extent of binding of biotinylated (and fluorophore tagged) oligonucleotides on the bead even under the best

possible mixing depend on several factors, e.g., the relative concentrations of the beads and the analyte, and the duration of incubation. The fluorescence emission per fluorophore is also dependent on the nature of the medium (e.g., PEG loading of the buffer solution). For calibration, 8 μl samples of the stock suspension ($\sim 4.3 \times 10^7$ beads) of magnetic bead are incubated with 1 nmol of Cy3-Oligo-Biotin samples at 0.1 nmol/μl concentrations (either in PBS or a 5 or 10% by mass PEG solution in PBS). After 30 min of incubation with repeated shaking, the conjugate samples are passed through the microchannel under the influence of the magnetic field. As the magnetic beads (with the surface-bound fluorophore) are collected in aggregates, the mean fluorescence intensity of the aggregates is computed from their epifluorescence images.

Figure 6 shows the variation of the average fluorescence intensity of the aggregates with the exposure time of captured images for three different PEG loading of the buffer. Average fluorescence intensities from the aggregates are evaluated (as described in Sect. 3.2) after the incubated bead suspension is flown through the stream B of microchannel (while streams A and C passed the buffer) for 10 min. In agreement with the exposure–intensity calibration of the camera, the fluorescence intensity vs. exposure time curves are linear. However, it is observed that the fluorescence intensity of the aggregate is nearly halved when the buffer has a 5 or 10% (by mass) PEG loading. The reduction of fluorescence is found to be more sensitive to the presence or absence of PEG in the buffer rather than the percentage of PEG. The latter can be explained through

Fig. 5 a Cy3 fluorescence image of cross-stream mixing of bead and oligonucleotide for two different inlet particle concentrations in stream B (the oligo concentration in stream C is fixed at 0.25 nmol/ml). The R1, R2, and R3 areas on the bead aggregate indicate the regions of interest for evaluating the average fluorescence intensity of the aggregate. The inset (*top*) shows an image of a part of the aggregate with the 50× objective (the vertical bar denotes 25 μm). **b** Growth of average fluorescence intensity of the aggregates with time. The average flow velocity is 579 μm/s
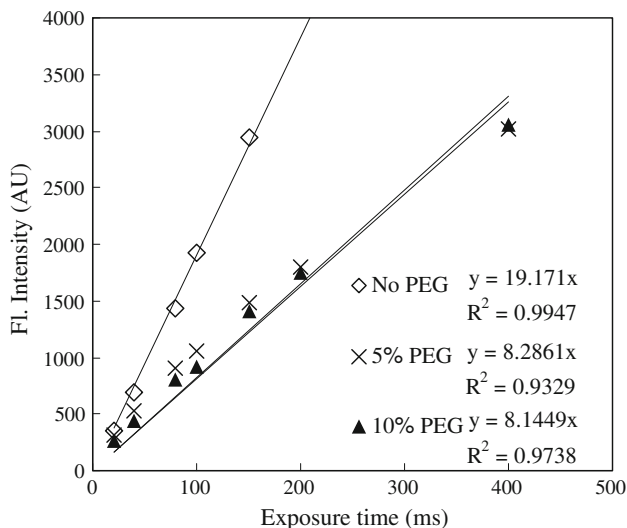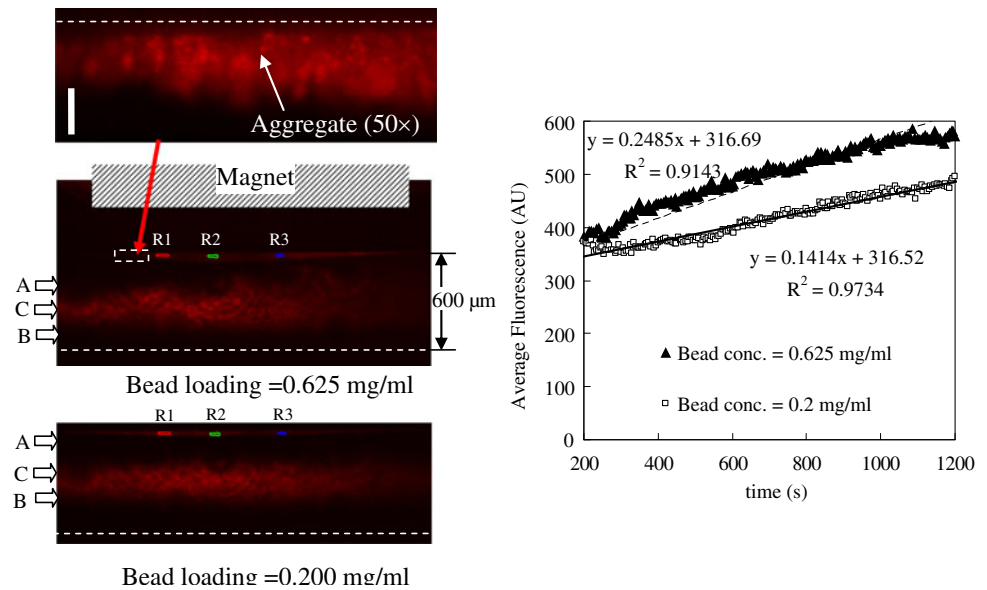
Fig. 6 Fluorescence intensity from separately (externally) incubated beads at an analyte concentration of 0.1 nmol/μl and different PEG loadings

the surfactant nature of PEG that is easily adsorbed to solid surfaces.

The extent of actual in situ streptavidin–biotin binding occurring on the beads inside the microchannel is expressed as a fraction of the ideal binding obtained through the prolonged incubation of beads and oligonucleotides (as described in the preceding paragraphs) at the same concentrations in a well-stirred aliquot. For example, any fluorescence intensity per pixel data is first corrected for the exposure time (of the camera used for the fluorescence imaging) and then adjusted for the "masking" effect due to PEG (at the same loading). The binding ratio is defined as the ratio of the fluorescence intensities exhibited by the

in situ incubated bead aggregate to the same from a pre-incubated bead aggregate under the identical camera exposure and PEG loading. For PEG loadings of 0, 5, and 10% (by mass), Fig. 6 provides the necessary calibration curves for the evaluation of the binding ratio.

3.4 Quantitative analysis of binding on the beads

3.4.1 Binding ratio in terms of fluorescence intensity

Although the fluorescence intensity of the aggregate is expected to vary with the residence time of the beads within the stream C as they move across the channel, an experimental determination of such residence time was not feasible. In principle, the residence time for one particle could be measured by "following" one particular particle, and repeating the procedure a large number of times for different particles. But Lagrangian tracking of individual particle was limited by the poor fluorescence intensity from an individual particle at 4× magnification. Fluorescence intensities are larger and particles are better visible using a 50× objective, but then the field of view is too small for reliable tracking. Instead, we followed a more deterministic approach of controlling the particle residence time (in stream C) by altering the width of the stream C using a conventional flow-focusing arrangement (Knight et al. 1998). The average flow velocity is maintained at 579 μm/s by keeping the sum of the flow rates of streams A, B, and C constant. The extent of streptavidin–biotin binding is evaluated (in terms of the binding ratio), and the influence of parameters such as the viscosity of the medium and the relative widths of the A, B, and C streams on it is then investigated.

Fig. 7 a–c Fluorescence images for different flow ratios of the A, B, and C streams for a total flow of 150 μl/h ($u_{av} = 579$ μm/s). **d** Binding ratio for different fractional flow rates of the Cy3 stream and different fluid viscosities (PEG loading in the PBS buffer). The *solid line* shows a nonlinear curvefit of the data
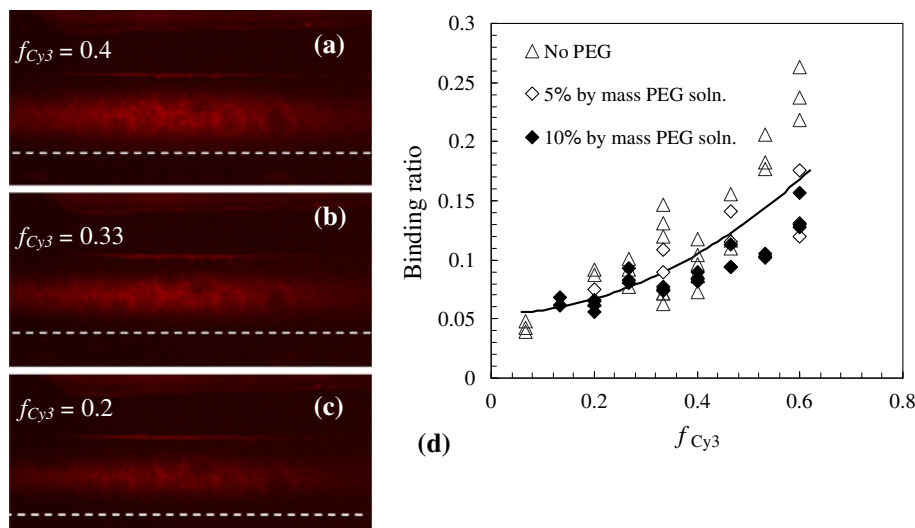

Figure 7a–c shows the fluorescence images of the test zone for three different f_{Cy3} values. As can be seen from Fig. 7a–c, the larger the fraction of the central Cy3 stream, the wider is the central fluorescent zone. As a consequence, the beads from the stream B spend a longer duration in the central stream and bind to the Cy3 labeled oligonucleotides through the biotin–streptavidin binding. The average pixel intensities of the aggregates are evaluated from the images using the same representative ROIs as discussed before. The pixel intensity is interpreted in terms of the binding ratio by dividing the computed average pixel intensity values with the saturation pixel intensity values of Fig. 6 corresponding to the same conditions of oligonucleotide concentration and PEG loading. Figure 7d shows that the binding ratio increases monotonically with f_{Cy3}. When the experiments are repeated with different PEG loadings, the data point merge within the zone of scatter. The scatter in the data is high at the large f_{Cy3} values, particularly with pure buffer (no PEG), when the viscosity is the lowest. At larger f_{Cy3} values, the mixing boundary layer of the central oligo-Cy3 stream approaches closer to the bead aggregate region. Thus, spurious carryover of fluorophores to the bead aggregate is more probable in the event of any small flow perturbation. This may have added to the fluorescence signal from the bead aggregate for some runs, and led to a large scatter at larger f_{Cy3} values. The scatter decreases as the viscosity increases (e.g., for 5 and 10% PEG). This can be attributed to both a more stable flow (less disturbance in flow), and a reduced diffusivity of the oligo-Cy3 conjugates at larger viscosities (less spurious carryover). At lower f_{Cy3} values the curves overlap distinctly. Figure 7d suggests that the binding ratio has a nonlinear dependence on the width of the Cy3 stream, and is relatively insensitive to the viscosity of the medium.

3.4.2 Scaling analysis

The observed behavior of the binding ratio can be explained through a scaling analysis that accounts for the magnetophoretic motion of particles and a diffusion-limited analyte binding in stream C. Figure 8a shows a schematic diagram of the trajectory of a magnetic bead as it traverses through the stream C of width h_{Cy3}. For the purpose of the scaling analysis, we assume an average magnetic force F_M on the particles as they move across the analyte stream, leading to an average magnetophoretic velocity $V_M = F_M/6\pi a\eta$ (Eq. 5). The transport of analyte from the bulk of the stream C to the bead surface can be explained through the assumption of a diffusion boundary layer around the spherical particle, with an adsorption boundary condition at the particle surface. The total analyte binding per bead can be evaluated from the knowledge of the mass transfer coefficient of the analyte to the spherical particle, and the particle residence time in the analyte stream. Considering $V_M \sim 1$ mm/s in the aqueous medium, the particle Reynolds number is of the order of $Re = 2V_m a/\eta \sim 10^{-3}$. Also, assuming the 22 base-pair oligonucleotides have a diffusivity $D = 5.3 \times 10^{-11}$ m²/s in water (Lukacs et al. 2000), the Péclet number associated with the diffusion boundary layer around a magnetic bead is $Pe = 2V_M a/D \sim 38$. The expression for the Sherwood number (Sh) for spherical particles in the relevant regime of Re and Pe is suggested by Crowe (2006) as:

$$Sh = 1.249\left(\frac{Pe}{2}\right)^{1/3} + 0.922, \text{ for } Re \ll 1, \text{ and } 5 < Pe. \quad (8)$$

Assuming an infinitely fast streptavidin–biotin binding kinetics (Huang et al. 1996) and an abundance in available binding sites on the bead surface, the analyte transfer rate

(a)

1: Particle at $t=t_0$
2: Particle at $t=t_0 + \tau_{Cy3}$

(b)
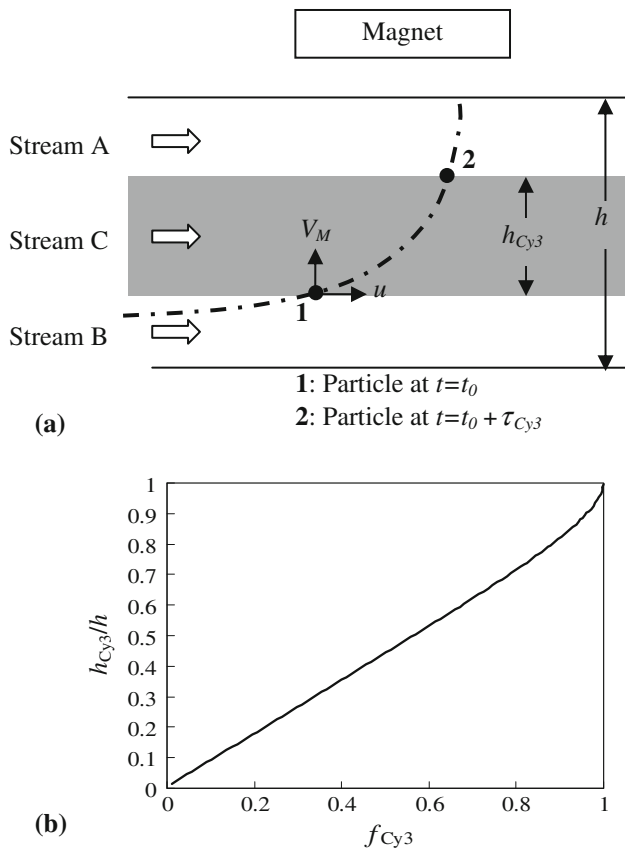
Fig. 8 a Schematic diagram for the movement of a magnetic microsphere through the stream C. h_{Cy3}: width of Cy3 stream C. 1 and 2 denote the location of a particle at two instants. b Relative width of the stream C as a function of the fractional Cy3 flow, computed from the velocity profile described in Eq. 6a

to a particle can be expressed in terms of its radius, the Sherwood number, and the concentration of the analyte as

$$\frac{dN_{bind}}{dt} = 2\pi C_{DNA} D \cdot a \cdot Sh, \tag{9}$$

where N_{bind} is the number of analyte molecules having bound to receptors on the particle's surface. Considering the large Pe asymptote of Sherwood number correlation (Eq. 8), i.e., $Sh \propto Pe^{1/3} = (2V_M a/D)^{1/3}$, the total analyte binding can be evaluated by time-integrating Eq. 9, for the residence time $\tau_{Cy3} = h_{Cy3}/V_M$ of the particle in stream C, i.e.,

$$N_{bind} \propto 2\pi C_{DNA} \cdot D \cdot a \cdot \int_0^{\tau_{Cy3}} (2V_M a/D)^{1/3} dt$$

$$\propto C_{DNA}(D/V_M)^{2/3} \cdot a^{4/3} \cdot V_M \cdot \tau_{Cy3}. \tag{10a}$$

The Stokes–Einstein equation relates the analyte diffusivity in the buffer to the effective hydrodynamic radius r_{hDNA} of the analyte (Cy3 labeled and biotinylated oligonucleotide) molecules and the viscosity of the medium as $D = kT/6\pi r_{hDNA}\eta$, where k denotes the

Boltzmann constant ($= 1.3807 \times 10^{-23}$ J/K). Thus, the analyte binding equation (10a) reduces to

$$N_{bind} \propto C_{DNA}(kT/r_{hDNA}F_M)^{2/3} \cdot a^2 \cdot h_{Cy3}. \tag{10b}$$

For a channel with a depth to width aspect ratio $b:h = 1:5$, the velocity profile, as described by Eq. 6a is nearly flat-topped in the wide direction. When this velocity profile is used to compute the relative width (h_{Cy3}/h) of the stream C as a function of the fractional Cy3 flow rate $f_{Cy3} = \int_{-\frac{1}{2}h_{Cy3}}^{\frac{1}{2}h_{Cy3}} \int_{-\frac{1}{2}b}^{\frac{1}{2}b} u(y,z) dy dz / \int_{-\frac{1}{2}h}^{\frac{1}{2}h} \int_{-\frac{1}{2}b}^{\frac{1}{2}b} u(y,z) dy dz$, a nearly linear relationship is obtained, as shown in Fig. 8b. Therefore, Eq. 10b can be approximately written as:

$$N_{bind} \propto C_{DNA}(kT/r_{hDNA}F_M)^{2/3} \cdot a^2 \cdot h \cdot f_{Cy3}. \tag{11a}$$

Equation 11a agrees with the experimental observation that the binding is independent of the host fluid viscosity. However, unlike the experimental finding (the trend-line of Fig. 7d), the dependence of analyte binding on the f_{Cy3} is linear in Eq. 11a. This can be explained from the fact that the magnetic force F_M across the cross section of the analyte stream is not constant in practice. The exact nature of F_M vs. y curve in the channel cannot be accounted for in a scaling analysis. However, if one assumes a spatial distribution of force as $F_M \propto y^{-n}$, the resulting magnetophoretic velocity would also vary with y, and substituting $dt = dy/V_M$, Eq. 10a reduces to:

$$N_{bind} \propto C_{DNA}(kT/r_{hDNA})^{2/3} \cdot a^2 \cdot \int_0^{h_{Cy3}} y^{2n/3} dy. \tag{11b}$$

Reckoning the nearly linear relationship between h_{Cy3} and f_{Cy3}, the expression for analyte binding takes the form:

$$N_{bind} \propto C_{DNA}(kT/r_{hDNA})^{2/3} \cdot a^2 \cdot h^{(1+2n/3)} \cdot f_{Cy3}^{(1+2n/3)}. \tag{11c}$$

Therefore, for any nonzero value of n, the relationship between N_{bind} and f_{Cy3} would be nonlinear.

3.4.3 Binding ratio in terms of numerically computed effective particle residence time

Although the foregoing scaling analysis shows that the average analyte binding per bead is independent of the fluid viscosity, a more accurate dependence of the binding on f_{Cy3} would require numerical computation of actual particle residence times in the central stream. The scaling analysis result (Eq. 11a) assumes a constant magnetic force F_M on the particles at all y locations. But the particles actually experience a spatially varying force-field, which is taken into consideration in the numerical prediction. The

magnetic force on the particles is evaluated based on the computed field distribution and the instantaneous locations of the particles as they travel along curved trajectories. Figure 9a and b shows the particle trajectories for $f_{Cy3} = 0.33$, and $f_{Cy3} = 0.9$, respectively, at an average host fluid velocity $u_{av} = 579$ μm/s. As can be seen from Fig. 9, the particle trajectories differ depending upon their initial position of release. Therefore, the residence time (in the middle stream) differ from particle-to-particle. For the purpose of quantitative comparison, the average residence time and its standard deviation are evaluated for the captured particles. Two salient effects of changing the flow fractions of the bead and analyte streams are apparent from Fig. 9. Firstly, as already pointed out in Fig. 8b, the width of stream C increases with increasing f_{Cy3}, which in turn increases the average residence time of the captured beads in that stream. Besides, a change in f_{Cy3} also leads to a change in the number of particles on the upper wall. At low values of f_{Cy3}, the bead stream is relatively wider. This enhances the possibility of the magnetic capture of beads, since a larger number of them pass closer to the magnet. For example, 35 of the 50 particles are captured by the magnet for $f_{Cy3} = 0.33$, implying that the test section has a particle capture efficiency CE = 70%. Magnetic beads are pushed further away from the magnet at larger value of f_{Cy3}, which reduces the capture efficiency of the particles (e.g., the particle capture efficiency is only 44% for $f_{Cy3} = 0.9$, see Fig. 9b).

Figure 10a shows the variation of the average residence time τ_{Cy3} of the particles in the central stream with f_{Cy3} for three different PEG loadings (percentage by mass) in the host fluid, e.g., 0, 5, and 10%. The corresponding viscosities of the background liquid, as obtained from the literature (Branca et al. 2002), are $\eta = 0.00089$, 0.00118, 0.00163 Pa·s, respectively. The vertical error bars in Fig. 10a denote the standard deviation of τ_{Cy3} for the captured particles. The average τ_{Cy3} increases with f_{Cy3}, and the variation is nonlinear. As the value of f_{Cy3} is increased, the central stream spreads more to both sides, and the interface between the central and the lower (bead) streams move further away from the magnet. Thus, as the particles enter the central stream during the transverse motion toward the upper wall, the initial magnetic force is weaker at large f_{Cy3}. Therefore, the particles spend progressively larger time at the higher values of f_{Cy3}, resulting in a gradually increasing slope of the residence time curves (Fig. 10a). Particles spend longer in the central stream at higher viscosity, since the overall time of transverse motion (to the wall) is increased. For example, at 10% PEG loading, the τ_{Cy3} values are, on an average, 1.6 times larger than that for 0% PEG case.

The transport of the analyte species to the bead surface is proportional to the mass diffusivity of the analyte in the background fluid (and hence, inversely proportional to its viscosity). If we assume a diffusion-limited binding of the analyte on the beads, the average analyte binding on each bead (which is analogous to the binding ratio discussed in Sect. 3.4.1) will be proportional to the product of the diffusivity-adjusted residence time ($\tau_{Cy3} \cdot D_0/D$), where D_0 denotes the diffusivity of the oligonucleotide molecule in the buffer with no PEG. When the diffusivity-adjusted residence time data are plotted against f_{Cy3}, they nearly coincide for the three viscosity values. This agrees with the trend of binding ratio as observed in Fig. 7d. Therefore, for the range of analyte concentrations investigated in Sect. 3.4.1, we can conclude that the analyte binding is

Fig. 9 Particle trajectories for **a** $f_{Cy3} = 0.33$, and **b** $f_{Cy3} = 0.9$. The host fluid does not contain any PEG. The flow rate corresponds to an average velocity of 579 μm/s. Fifty particles are released from random locations in the inlet to represent a homogeneous particle suspension

(a)

(b)
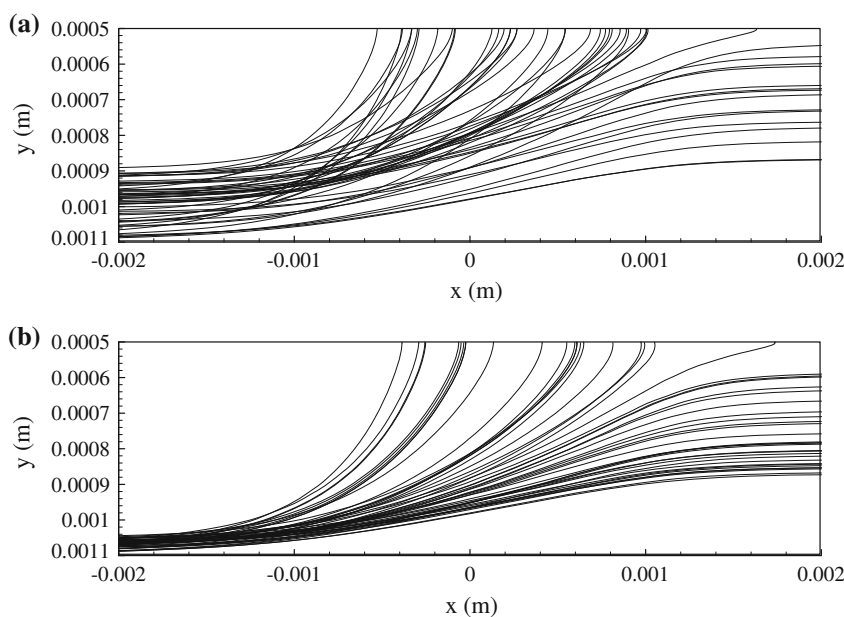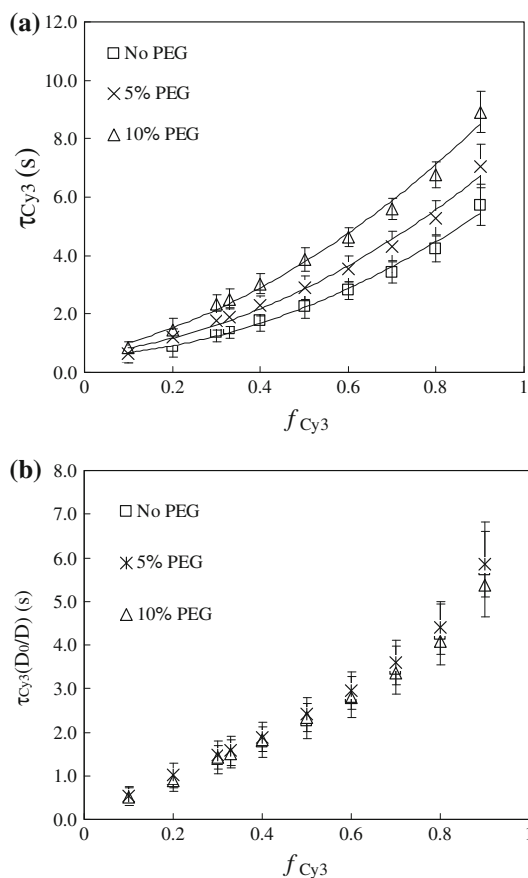
Fig. 10 Variation of **a** the mean particle residence time in the stream C, as a function of f_{Cy3} at different PEG loading in the host fluid. **b** The diffusivity-adjusted particle residence time curves for all the viscosity values collapse to a single curve. Vertical error bar denote the variance of particle residence times for an ensemble of 50 particles

diffusion-limited. This corroborates the findings of Huang et al. (1996) who observed that for a similar heterogeneous immunoassay (streptavidin-coated polystyrene microspheres and biotinylated DNA), the biotin–streptavidin binding kinetics is very fast, and the actual rate of binding is diffusion-limited.

3.5 Device optimization based on the numerical prediction

For magnetic bead-based biosensing applications, the analyte concentration is generally very small. For such devices, the signal-to-noise ratio of detection depends on the extent of immunochemical binding of analyte on each bead. Therefore, Figs. 7d and 10b provide a relative estimate of device sensitivity as function of the parameter f_{Cy3}. From the experimental and numerical results it is evident that the sensitivity of a biosensing device, which implements the proposed in situ bead incubation system, will be

independent of the fluid viscosity, and will increases with increased f_{Cy3}. However, for immunomagnetic separation applications where the total number of magnetic beads as well as the count of target analyte molecules (or cells) is limited, one has to consider both the average analyte binding per bead and the bead capture efficiency. Since the total quantity of immunochemically separated analyte in such a device is the product of the average analyte binding per bead and the total number of beads captured, the relative performance of the separator can be evaluated in terms of the product (CE $\cdot$ τ_{Cy3} $\cdot$ D_0/D), where CE denotes the particle capture efficiency (the ratio of magnetically captured particles to the total number of particles considered at the channel inlet). Figure 11a shows the variation of bead capture efficiency with f_{Cy3} for three different viscosities of the host fluid. As apparent from the particle trajectories of Fig. 9, the value of CE decreases with f_{Cy3}. This makes the total analyte capture (proportional to (CE $\cdot$ τ_{Cy3} $\cdot$ D_0/D)) vs. f_{Cy3} plots of Fig. 11b less steep than the plots of the average binding per bead (Fig. 10b). Also, Fig. 11a shows that the capture efficiency is lower at higher host fluid viscosity values, since the increased viscous drag in a larger number of particles is then able to overcome the transverse magnetic force, leading to a larger number of particles escaping downstream. Since the CE vs. f_{Cy3} plots follow three different curves at three different viscosities (Fig. 11a), the values of the product (CE $\cdot$ τ_{Cy3} $\cdot$ D_0/D) also show a dependence on the fluid viscosity (see Fig. 11b). Thus, the total analyte collection is the highest at the lowermost viscosity.

For high-throughput collection, where the total analyte collection rate is more important, one has to consider the total flow rate of beads, the bead collection efficiency of the separator, as well as the per-bead binding of analyte. If a homogeneous suspension is used, the overall analyte capture rate is proportional to (f_{Bead} $\cdot$ CE $\cdot$ τ_{Cy3} $\cdot$ D_0/D) = [CE $\cdot$ τ_{Cy3} $\cdot$ (D_0/D){0.5(1 − f_{Cy3})}], where the fractional bead stream flow rate is given by f_{Bead} = {0.5(1 − f_{Cy3})} for the proposed flow arrangement. Since the value of f_{Bead} decreases linearly with f_{Cy3}, the product (f_{Bead} $\cdot$ CE $\cdot$ τ_{Cy3} $\cdot$ D_0/D) first increases with f_{Cy3}, assumes a maximum at an intermediate value and then decreases with further increase of f_{Cy3}. Figure 11c shows that for all three PEG loadings (i.e., 0, 5, and 10% by mass) of the host fluid, the maximum analyte collection rate is observed between 0.4 $\leq$ f_{Cy3} $\leq$ 0.5 for the same average total flow rate of Fig. 10.

The effect of a variation of flow velocity on the immunomagnetic binding is also studied from the same perspective, and the results for a given viscosity (=0.00098 Pa·s) and f_{Cy3} (=0.33) are summarized in Fig. 12. It is apparent from Fig. 12a that the mean value of τ_{Cy3} decreases with velocity, although the dependence is weak. At higher velocities, a larger number of beads that
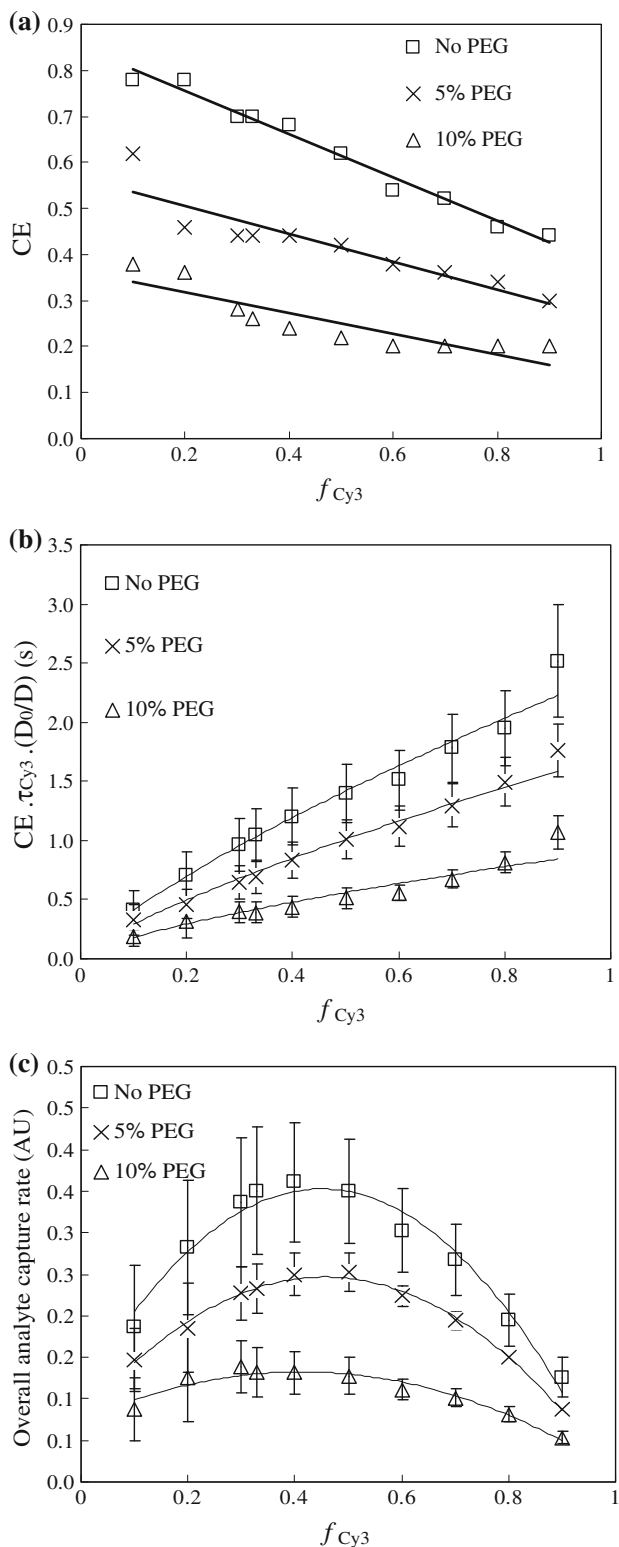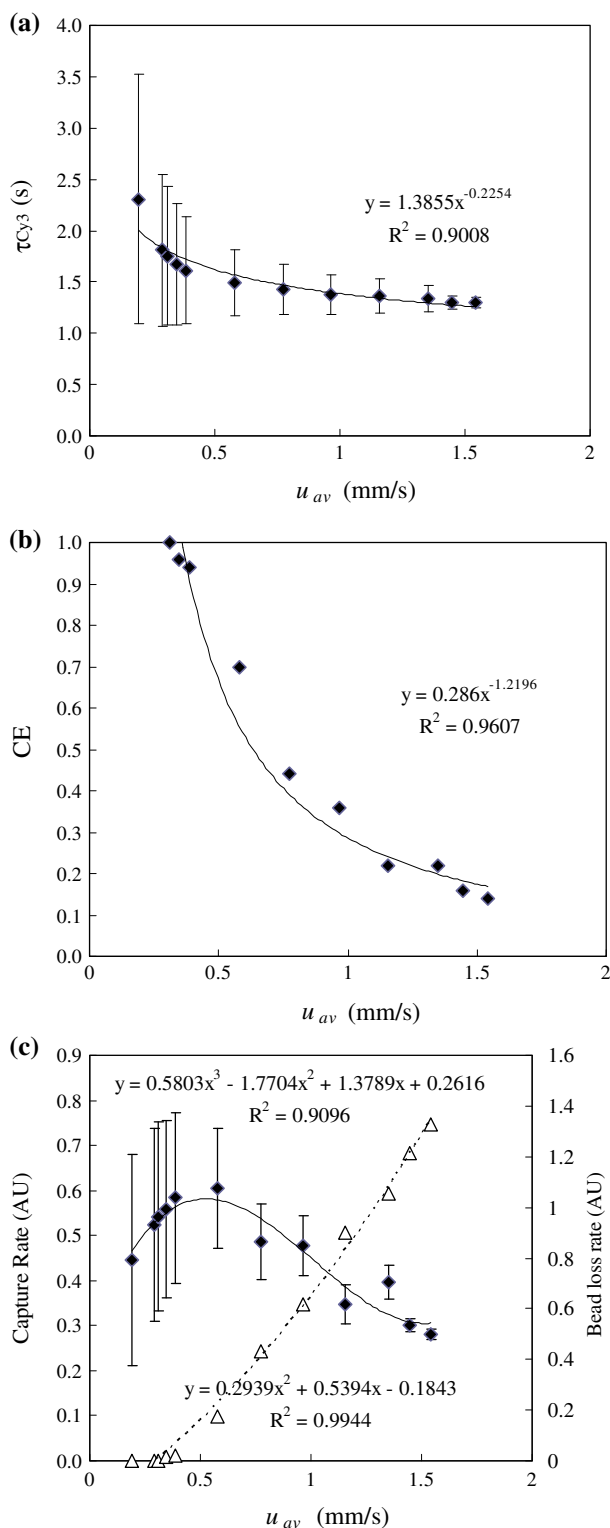
Fig. 11 **a** Variation of CE with f_{Cy3}. **b** The product $\{CE \cdot \tau_{Cy3} \cdot (D_0/D)\}$, denoting the overall quantity of immunochemically separated target molecules, as a function of f_{Cy3}. **c** Overall analyte capture rate $\propto$ $[CE \cdot \tau_{Cy3} \cdot (D_0/D) \cdot \{(1 - f_{Cy3})/2\}]$ plotted as function of f_{Cy3}

experience a lower magnetophoretic force (and hence take longer to pass the stream C) evade the capture. This, in effect, leads to the reduction of average bead residence time. The standard deviation of τ_{Cy3}, on the other hand, drops remarkably at larger velocity, since the increased drag at higher velocity leads to a "natural selection" of particles, capturing only those that are within a narrow range of stronger magnetic influence. The capture efficiency, as can be seen from the Fig. 12b, drops steeply with increased velocity. Since both τ_{Cy3} and CE drop with increased velocity, the product $(CE \cdot \tau_{Cy3} \cdot D_0/D)$, representing the total analyte capture from a specified volume of sample, also drops monotonically with velocity. However, the overall analyte capture rate, which is proportional to the product $\{CE \cdot \tau_{Cy3} \cdot (D_0/D) \cdot (u_{av})\}$, shows an increasing trend for up to $u_{av} = 0.58$ mm/s, above which it decreases again (Fig. 12c). For the chosen value of viscosity and f_{Cy3}, the optimum average flow velocity for the largest analyte capture rate is found to be 0.58 mm/s. Any operating velocity beyond this is highly undesirable, since it also associates with a large loss rate $(\{(1 - CE) \cdot (u_{av})\})$ of non-captured magnetic particles from the test section. Figure 12c shows that the bead loss is nearly zero (primarily due to a very high CE) until an operating average velocity of 0.38 mm/s, above which the loss rate increases sharply. In the velocity range $0.38 \leq u_{av} \leq 0.58$ mm/s, any gain in analyte capture rate would occur at the expense of increased bead loss rate, and the choice of operating flow rate would depend on the relative cost of the beads and the analyte. For high-throughput applications with large bead loading, the device performance can be affected if the bead aggregate grows large enough to alter the flow profile. However, the aggregate growth in a straight channel will cease at a critical aggregate size (Sinha et al. 2009) (when the particle loss due to the fluid drag from the outer periphery of the aggregate balances the bead collection rate) and the proposed scheme can still work without clogging the channel.

4 Conclusions

In situ immunochemical binding of biotinylated oligonucleotides on streptavidin-coated magnetic beads has been performed through magnetophoresis-aided cross-stream mixing in a microfluidic channel. The extent of binding on each bead was evaluated experimentally through fluorescence imaging of the bead–oligonucleotide conjugates that are magnetically separated in the microchannel. The extent of immunochemical binding under different flow ratios of the fluid streams and viscosities of the background fluid

(a)

$$y = 1.3855x^{-0.2254}$$
$$R^2 = 0.9008$$

(b)

$$y = 0.286x^{-1.2196}$$
$$R^2 = 0.9607$$

(c)

$$y = 0.5803x^3 - 1.7704x^2 + 1.3789x + 0.2616$$
$$R^2 = 0.9096$$

$$y = 0.2939x^2 + 0.5394x - 0.1843$$
$$R^2 = 0.9944$$

Fig. 12 Effect of flow velocity u_{av} on **a** the residence time of captured particles in the stream C, **b** the capture efficiency, and **c** the capture rate of the analyte (*filled diamond*) as a function of u_{av}. In addition, frame (**c**) shows the bead loss rate (*open triangle*) (defined as $\{(1 - CE) \cdot (u_{av})\}$). The host fluid does not contain any PEG, and $f_{Cy3} = 0.33$

were compared. The analyte binding per bead was found to be monotonically increasing with the analyte flow volume fraction, but independent of the fluid viscosity. A diffusion-based binding analysis, which relates the extent of binding to the diffusivity-adjusted residence times of the beads in the analyte stream, was found to agree with the experimentally observed trend of binding ratio. For biosensing applications, where the analyte binding per bead is of primary practical relevance, the background fluid viscosity was found to have no influence. However, the same is not true for a separator where the overall count of separated analyte is important. For a fixed flow condition, the capture efficiencies of the beads decline and the overall analyte capture decreases with an increase in the fluid viscosity. The bead residence time in the analyte stream exhibits a weakly decreasing trend, accompanied by a strong decline in bead capture efficiency with increased flow velocity. For high-throughput devices, where the analyte separation rate is of highest importance, the overall analyte binding rate was found to maximize within an optimum regime of flow velocity and analyte flow fraction. Besides the flow parameters and the fluid properties, the device performance is also expected to depend on the dipole strength of the magnet, the particle size and their magnetic susceptibility. The general features of particle trajectories will, however, remain as reported here, as long as the ratio of magnetic force to viscous force on a particle remains the same.

References

Baier T, Mohanty S, Drese KS, Rampf F, Kim J, Schönfeld F (2009) Modelling immunomagnetic cell capture in CFD. Microfluid Nanofluid 7:205–216

Biswal SL, Gast AP (2004) Micromixing with linked chains of paramagnetic particles. Anal Chem 76:6448–6455

Branca C, Magazu S, Maisano G, Migliardo F, Romeo G (2002) Hydration study of PEG/water mixture by quasi elastic light scattering, acoustic and rheological measurements. J Phys Chem B 106:10272–10276

Crowe CT (2006) Multiphase flow handbook. Taylor and Francis, Boca Raton, FL

Ganguly R, Puri IK (2007) Field-assisted self-assembly of superparamagnetic nanoparticles for biomedical, MEMS and BioMEMS applications. Adv Appl Mech 41:293–335

Graham DL, Ferreira HA, Freitas PP (2004) Magnetoresistive-based biosensors and biochips. Trends Biotechnol 22:455–462

Greenwood PA, Greenway GM (2002) Sample manipulation in micro total analytical systems. Trends Anal Chem 21:726–740

Hardt S, Pennemann H, Schönfeld F (2006) Theoretical and experimental characterization of a low-Reynolds number split-and-recombine mixer. Microfluid Nanofluid 2:237–248

Hayes MA, Polson NA, Phayre AN, Garcia AA (2001) Flow-based microimmunoassay. Anal Chem 73:5896–5902

Huang S-C, Stump MD, Weiss R, Caldwell KD (1996) Binding of biotinylated DNA to streptavidin-coated polystyrene latex: effect of chain length and particle size. Anal Biochem 237:115–122

Ichikawa N, Hosokawa K, Maeda R (2004) Interface motion of capillary-driven flow in rectangular microchannel. J Colloid Interf Sci 280:155–164

Jiang F, Drese KS, Hardt S, Küpper M, Schönfeld F (2004) Helical flows and chaotic mixing in curved micro channels. AIChE J 50:2297–2305

Kang Y, Cetin B, Wu Z, Li D (2009) Continuous particle separation with localized AC-dielectrophoresis using embedded electrodes and an insulating hurdle. Electrochimia Acta 54:1715–1720

Kang Y, Li D, Kalams SA, Eid JE (2008) DC-dielectrophoretic separation of biological cells by size. Biomed Microdevices 10:243–249

Knight JB, Vishwanath A, Brody JP, Austin RH (1998) Hydrodynamic focusing on a silicon chip: mixing nanoliters in microseconds. Phys Rev Lett 80:3863–3866

Lacharme F, Vandevyver C, Gijs MAM (2008) Full on-chip nanoliter immunoassay by geometrical magnetic trapping of nanoparticle chains. Anal Chem 80:2905–2910

Lacharme F, Vandevyver C, Gijs MAM (2009) Magnetic beads retention device for sandwich immunoassay: comparison of off-chip and on-chip antibody incubation. Microfluid Nanofluid (Article in Press). doi:10.1007/s10404-009-0424-7

Lukacs GL, Haggie P, Seksek O, Lechardeur D, Freedman N, Verkman AS (2000) Size-dependent DNA mobility in cytoplasm and nucleus. J Biol Chem 275:1625–1629

Lund-Olesen T, Buus BB, Howalt JG, Hansen MF (2008) Magnetic bead micromixer: influence of magnetic element geometry and field amplitude. J Appl Phys 103:07E902(1–3)

Manz A, Graber N, Widmer HM (1990) Miniaturized total chemical analysis systems: a novel concept for chemical sensing. Sens Actuators B Chem 1:244–248

Modak N, Datta A, Ganguly R (2009) Cell separation in a microfluidic channel using magnetic microspheres. Microfluid Nanofluid 6:647–660

Morton KJ, Loutherback K, Inglis DW, Tsui OK, Sturm JC, Chou SY, Austin RH (2008) Crossing microfluidic streamlines to lyse, label and wash cells. Lab Chip 8:1448–1453

Moser Y, Lehnert T, Gijs MAM (2009) Quadrupolar magnetic actuation of superparamagnetic particles for enhancedmicrofluidic perfusion. Appl Phys Lett 94:022505(1–3)

Mullins JM (1999) Overview of fluorophores. In: Javois LC (ed) Immunocytochemical methods and protocols, 2nd edn. (Vol. 34 of Biomedical and life sciences). Humana Press, Totowa, NJ, pp 107–116

Nandy K, Chaudhuri S, Ganguly R, Puri IK (2008) Analytical model for the magnetophoretic capture of magnetic microspheres in microfluidic devices. J Magn Magn Mater 320:1398–1405

Nguyen N-T, Wu Z (2005) Micromixers—a review. J Micromech Microeng 15:R1–R16

Pamme N, Manz A (2004) On-chip free-flow magnetophoresis: continuous flow separation of magnetic particles and agglomerates. Anal Chem 76:7250–7256

Radbruch A, Mechtold B, Thiel A, Miltenyi S, Pfluger E (1994) High-gradient magnetic cell sorting. Methods Cell Biol 42:387–403

Rida A, Gijs MAM (2004) Manipulation of self-assembled structures of magnetic beads for microfluidic mixing and assaying. Anal Chem 76:6239–6246

Rong R, Choi J-W, Ahn CH (2006) An on-chip magnetic bead separator for bio-cell sorting. J Micromech Microeng 16:2783–2790

Roy T, Chakraborty S, Sinha A, Ganguly R, Puri IK (2009) Magnetic microsphere-based mixers for micro-droplets. Phys Fluids 21:027101(1–7)

Sinha A, Ganguly R, De AK, Puri IK (2007) Single magnetic particle dynamics in a microchannel. Phys Fluids 19:117102(1–5)

Sinha A, Ganguly R, Puri IK (2009) Magnetic separation from superparamagnetic particle suspensions. J Magn Magn Mater 321:2251–2256

Smistrup K, Hansen O, Bruus H, Hansen MF (2005) Magnetic separation in microfluidic systems using microfabricated electromagnets—experiments and simulations. J Magn Magn Mater 293:597–604

Suzuki H, Ho C-M, Kasagi N (2004) A chaotic mixer for magnetic bead-based micro cell sorter. J Microelectromech Syst 13:779–790

Tibbe AGJ, de Grooth BG, Greve J, Dolan GJ, Rao C, Terstappen LWMM (2002) Magnetic field design for selecting and aligning immunomagnetic labeled cells. Cytometry 47:163–172

Wang Y, Zhe J, Chung BTF, Dutta P (2008) A rapid magnetic particle driven Microstirrer. Microfluid Nanofluid 4:375–389

Wu Z, Li D (2008) Micromixing using induced-charge electrokinetic flow. Electrochim Acta 53:5827–5835

Xia N, Hunt TP, Mayers BT, Alsberg E, Whitesides GM, Westervelt RM, Ingber DE (2006) Combined microfluidic-micromagnetic separation of living cells in continuous flow. Biomed Microdevices 8:299–308

Yung CW, Fiering J, Mueller AJ, Ingber DE (2009) Micromagnetic—microfluidic blood cleansing device. Lab Chip 9:1171–1177